Intermetallics 76 (2016) 18–25

Contents lists available at ScienceDirect

Intermetallics

journal homepage: www.elsevier.com/locate/intermet

New Fe-based soft magnetic amorphous alloys with high saturation magnetization and good corrosion resistance for dust core application

Y. Han [a], F.L. Kong [b], F.F. Han [a], A. Inoue [a, b, c, *], S.L. Zhu [a], E. Shalaan [c], F. Al-Marzouki [c]

[a] School of Materials Science and Engineering, Tianjin University, Tianjin 300072, China
[b] International Institute of Green Materials, Josai International University, Togane 283-8555, Japan
[c] Department of Physics, King Abdulaziz University, Jeddah 22254, Saudi Arabia

ARTICLE INFO

Article history:
Received 4 December 2015
Received in revised form
16 May 2016
Accepted 30 May 2016
Available online 22 June 2016

Keywords:
Soft magnetic alloy
Amorphous alloy
Corrosion resistance
Structural relaxation

ABSTRACT

Fe-rich amorphous dust core alloys with minor-addition of Mo and/or Cr were synthesized because of the industrial request of mass production of high efficient low core loss Fe-based dust cores. It was found that the present Fe-(Cr, Mo)-P-B-Si-(C) amorphous alloy ribbons exhibit good soft magnetic properties of above 1.5 T for saturation magnetization, below 10 A/m for coercivity and rather good corrosion resistance in 3%NaCl aqueous solution. Besides, the amorphous alloy ribbons exhibit good bending ductility in as-spun and optimally annealed states. It is noticed that these characteristics are much superior to those for commercial Fe-Cr-Nb-P-B-Si soft magnetic dust core alloy (SENNTIX). In addition, the annealing treatment was noticed to cause the improvement of corrosion resistance without detriment to bending ductility. The new Fe-based soft magnetic alloys with good combined characteristics are expected to be used as the basic material as high-efficient soft magnetic dust cores in a high frequency range.

1. Introduction

For the last several decades, the syntheses of Fe-based amorphous and nanocrystalline alloys with high amorphous-forming ability and good fundamental properties have been well carried out for applications as soft magnetic materials, owing to the expectations of low coercivity (H_c), high permeability and low cores loss [1,2]. In the recent high needs of high-efficient electric-magnetic devices, Fe-based soft magnetic dust cores, which can be used in a high frequency range and high current density, have attracted rapidly increasing interest. In the application to the high-efficient dust cores, the necessary basic characteristics are good soft magnetic properties, high saturation magnetization, high electrical resistivity, high corrosion resistance and high amorphous or glassy formation ability in conjunction with good production ability of amorphous or glassy alloy powders by water atomization [3]. In addition, high resistance of alloy liquid to oxidation is also required. These necessities are due to the inexpensive simple production process consisting mainly of water atomization, mixing of alloy powder and resin, cold consolidation instead of melt spinning process leading to the production of ribbon form.

As commercial dust core materials, the first application was Fe-Cr-P-B-Si-C alloy with the trademark of Liqualloy in 2002 [4], followed by Fe-Cr-Nb-P-B-Si alloy with SENNTIX in 2008 [5]. For such alloys, the Fe-based dust core materials always contain Cr and Nb elements leading to the improvement of corrosion resistance and oxidation resistance. Subsequently, a series of Fe-rich Cr/Nb-adopted alloy was synthesized in our very recent work [6]. Among them, several amorphous alloys were found to exhibit high saturation magnetizations near 1.5 T and better corrosion resistance than that of the Fe-rich Fe-metalloid amorphous alloys [7].

However, the dissolution of Cr and/or Nb causes a decrease in saturation magnetization. It is thus important to develop a new type of Fe-based dust core magnetic material with higher saturation magnetization, good corrosion resistance and good bending ductility as well as high amorphous-forming ability which enables the use of mass-production water atomization process. This paper aims to examine amorphous-forming ability, structural feature, thermal stability, mechanical properties, soft magnetic properties and corrosion resistance for Fe-Mo-P-B-Si-(C) and Fe-Cr-P-B-Si-(C) alloy ribbons in as-spun and annealed states and to investigate the feature of the new Fe-based amorphous alloys. In addition, we have noticed that the annealing treatment causes the improvement of corrosion resistance. The mechanism for the improvement is also

* Corresponding author. School of Materials Science and Engineering, Tianjin University, Tianjin 300072, China.
E-mail address: ainouebmg@yahoo.co.jp (A. Inoue).

http://dx.doi.org/10.1016/j.intermet.2016.05.011
0966-9795/

investigated from the views of surface performance and potential energy.

2. Experiment procedure

By optimization of alloy compositions, we chose $Fe_{84-x}C_xM_2B_8Si_2P_4$ (M = Cr or Mo; x = 0, 1) for the present study. The alloy compositions are represented by nominal atomic percentage. Their master alloy ingots were prepared by arc melting the mixtures of pure element of Fe, Si, B, Cr, Mo as well as Fe_3P and Fe-C alloy (99.99 mass%) in an argon atmosphere by high-frequency induction melting. Rapidly solidified ribbons were prepared by melt spinning with a copper wheel of 250 mm in diameter. The outer surface velocity of the wheel was about 40 m/s and the resulting alloy ribbons have a thickness of about 20 μm and a width of about 0.8–1.0 mm. The structure was examined by X-ray diffraction (XRD) with Cu-Kα radiation and transmission electron microscopy (TEM). Thermal stability was studied by differential scanning calorimetry (DSC) at a heating rate of 0.67 K/s. Bending ductility was evaluated by bending the ribbon specimen through 180°. Hardness was measured with a Vickers hardness tester with a load of 0.98 N (100 gf) for 10 s. The B_s and H_c were measured with a vibrating sample magnetometer (VSM) under a field of 800 kA/m and a DC B-H loop tracer under a field of 800 A/m, respectively.

Corrosion behaviors were evaluated by the samples which were degreased, washed and dried in air before electrochemistry test. Electrochemistry measurements were performed by an electrochemistry workshop (Gamry Reference 600 redefining electrochemical measurement) in 3.5 mass% NaCl solution at 298 K. Ribbon samples were set as working electrode; a platinum electrode was working as counter electrode and a saturated calomel electrode (SCE) was used as reference electrode. Polarization curves were measured by a potentiodynamic process from 200 mV under open circuit potential (OCP) to 1000 mV above OCP value at a scanning rate of 1 mV/s. Electrochemistry Impedance Spectra (EIS) tests were performed with signal amplitude of 10 mV around OCP values in the frequency range of 0.01–100,000 Hz. XPS data were collected by a monochromatized Al-Ka radiation. The surface of alloy ribbons was examined by scanning electron microscopy (SEM) with an additional energy-dispersive X-ray (EDX) device. Surface roughness is observed by a Bruker atomic force microscope (AFM).

3. Results and discussion

Fig. 1 shows XRD patterns of the $Fe_{84-x}C_xM_2B_8Si_2P_4$ (M = Cr or Mo; x = 0, 1) alloy ribbons. No sharp crystalline peak can be clearly recognized in these patterns, indicating the formation of an amorphous phase. Fig. 2 shows DSC curves of the present Fe-based alloy ribbons. The onset temperatures of the first and the second exothermic peaks (T_{x1} and T_{x2}) obtained from Fig. 2 are summarized in Table 1. For each curve, two separated exothermic peaks can be recognized, indicating the two-stage crystallization behavior. In order to clarify the precipitation phases, the structures of the alloys annealed under different conditions were examined by XRD and TEM. Fig. 3(a) shows the XRD patterns of exemplified $Fe_{83}Cr_2C_1B_8Si_2P_4$ alloy annealed at 773 K and 873 K for 600 s. The three peaks are seen in each diffraction pattern and can be indexed as bcc-Fe structure. In addition, tiny peak near 44 deg can be recognized for the alloy after annealing at 873 K, indicating the precipitation of Fe-B compound phases [8]. Fig. 3(b) and (c) show bright-field TEM images and the corresponding SAED patterns. Sharp rings in Fig. 3(c) can be indexed as (110), (200), (211) and etc of bcc-Fe, while other spots of the compound phase can be recognized. HR-TEM of the two phases was observed to clarify the structure in detail (Fig. 3(d) and (e)). For the compound phase, the interplanar crystal spacing (d) measured from two different directions are $d_1 = 0.112$ nm and $d_2 = 0.110$ nm. The corresponding Miller indices are determined (marked in Fig. 3(e)) and the

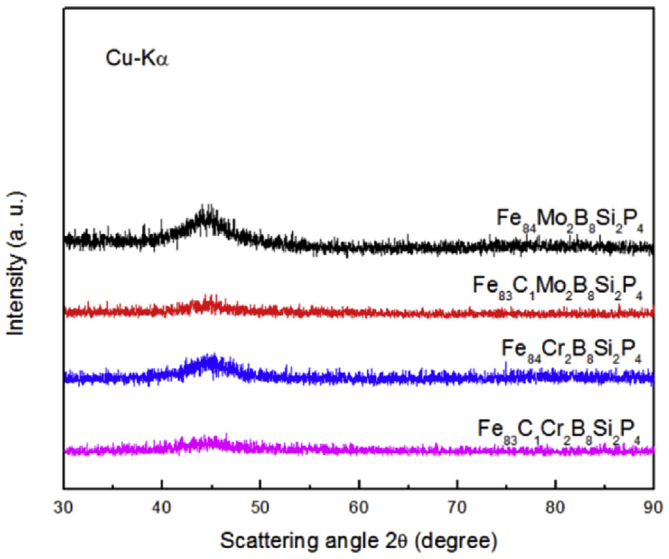

Fig. 1. XRD patterns of melt-spun $Fe_{84-x}C_xM_2B_8Si_2P_4$ (x = 0, 1; M = Mo and Cr) alloy ribbons.

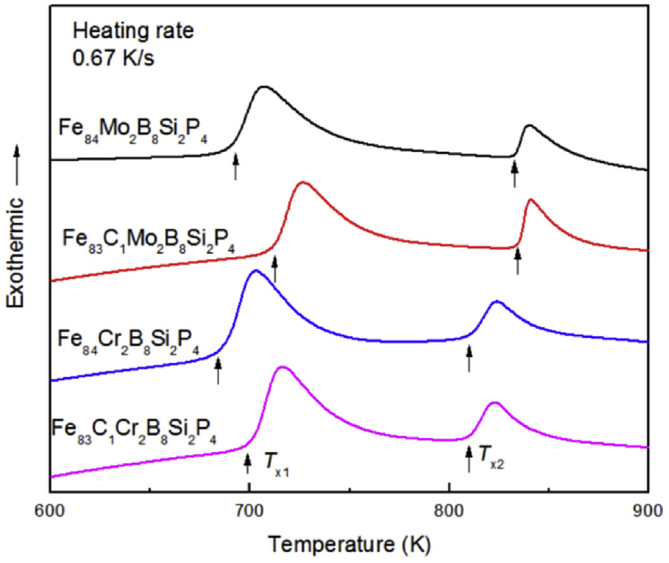

Fig. 2. DSC curves of melt-spun $Fe_{84-x}C_xM_2B_8Si_2P_4$ (x = 0, 1; M = Mo and Cr) alloy ribbons with a heating rate of 0.67 K/s.

Table 1
Crystalline onset temperature (T_{x1} and T_{x2}) of the as-spun $Fe_{84-x}C_xM_2B_8Si_2P_4$ (x = 0, 1; M = Mo and Cr) alloys and Vickers' hardness (H_V), saturation flux density (B_s) and coercivity (H_c) of these alloys annealed at each T_{x1}-100 K for 600 s. The data of SENNTIX alloy $Fe_{77}B_{9.5}P_{10.5}Nb_2Cr_1$ are shown together for comparison.

Composition	T_{x1} (K)	T_{x2} (K)	H_V (HV 0.05)	B_s (T)	H_c (A/m)
$Fe_{84}Mo_2B_8Si_2P_4$	693	833	929	1.53	7.308
$Fe_{83}Mo_2B_8Si_2P_4C_1$	712	834	938	1.51	4.604
$Fe_{84}Cr_2B_8Si_2P_4$	689	811	912	1.50	9.122
$Fe_{83}Cr_2B_8Si_2P_4C_1$	700	810	925	1.45	6.863
$Fe_{77}B_{9.5}P_{10.5}Nb_2Cr_1$ [5]	719	–	–	1.30	3.8

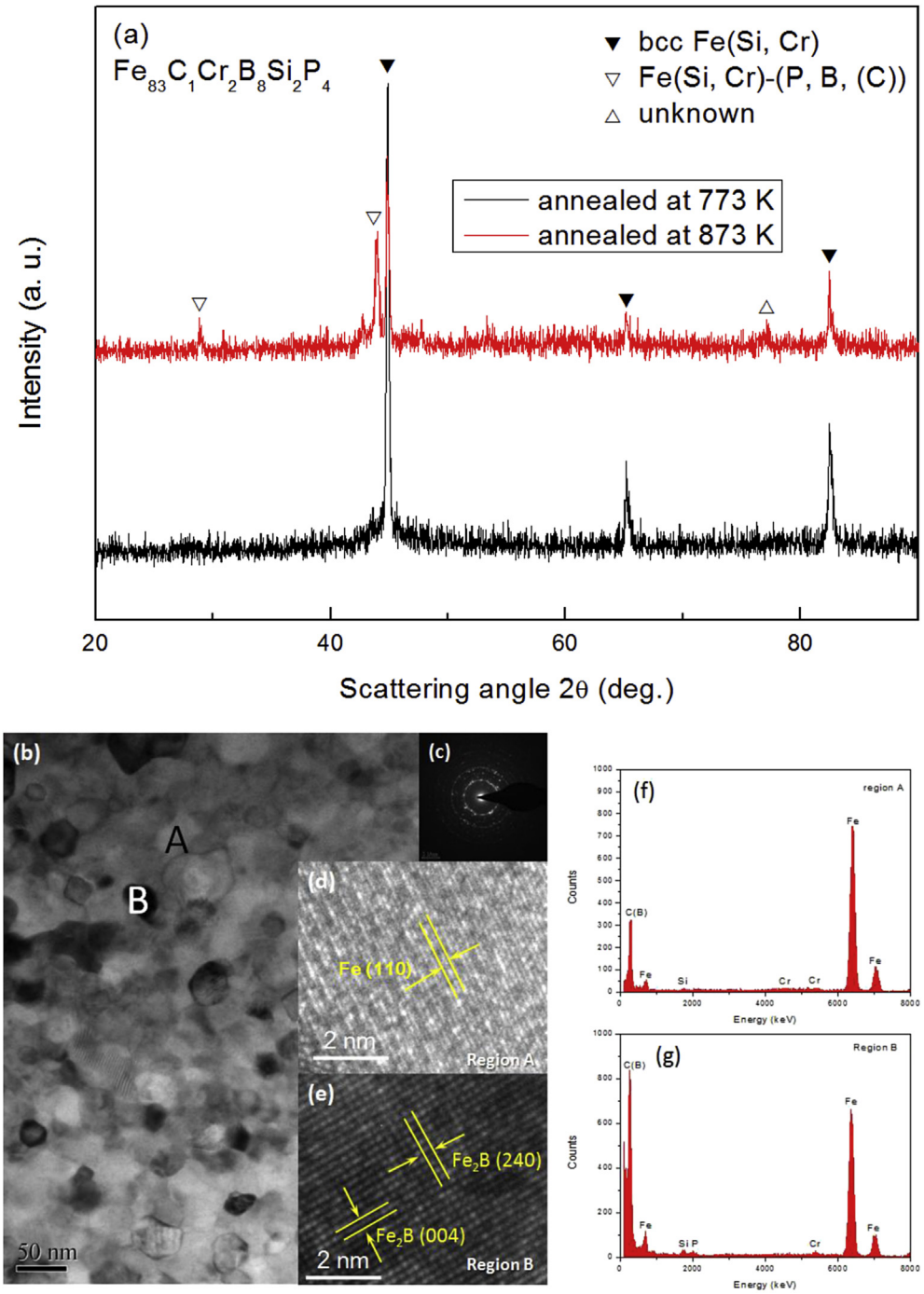

Fig. 3. (a) XRD patterns of $Fe_{83}C_1Cr_2$ $B_8Si_2P_4$ alloy ribbon annealed at 773 K and 873 K for 600 s (b) TEM bright-field image and (c) corresponding selected area electron diffraction pattern. (d) (e) High resolution TEM images and (f) (g) corresponding EDX spectra detected from region A and B in (a) for the $Fe_{83}C_1Cr_2B_8Si_2P_4$ alloy annealed at 873 K.

compound phase is indexed as tetragonal Fe_2B. Besides, it is noticed that the *d* values for bcc-Fe and Fe_2B are slightly larger than that of the reference values, indicating the solution of other elements in the lattice structure. The solute atoms were detected by EDX and shown in Fig. 3(f) and (g). Si and Cr elements can be detected with simultaneous presence of Fe element because of their solution in bcc-Fe and tetragonal Fe_2B lattice, while P elements can be only recognized in tetragonal Fe_2B lattice, which results from the substitution of B by P. Boron is not easy to distinguish from carbon by EDX, thus the peaks around 200 keV are marked as C(B). The two phases therefore can be identified as bcc-Fe(Si, Cr) phase and tetragonal Fe(Cr, Si)-metalloid (B,P, (C)) phase, respectively.

Thus, the first peak at the lower temperature side is due to the precipitation of bcc-Fe(Si, TM) phase, while the second one at the higher temperature side is associated with the precipitation of bcc-Fe(Si, TM) and tetragonal Fe(Si, TM)-metalloid compound from the remaining amorphous phase, which is similar as the results of Fe-metalloid alloys [8]. Besides, one can further notice that the onset temperatures of crystallization are dependent on composition. Their temperatures tend to increase for the alloys containing Mo or Cr element, indicating the improvement of thermal stability.

All the present alloy ribbons are ductile, and their bending

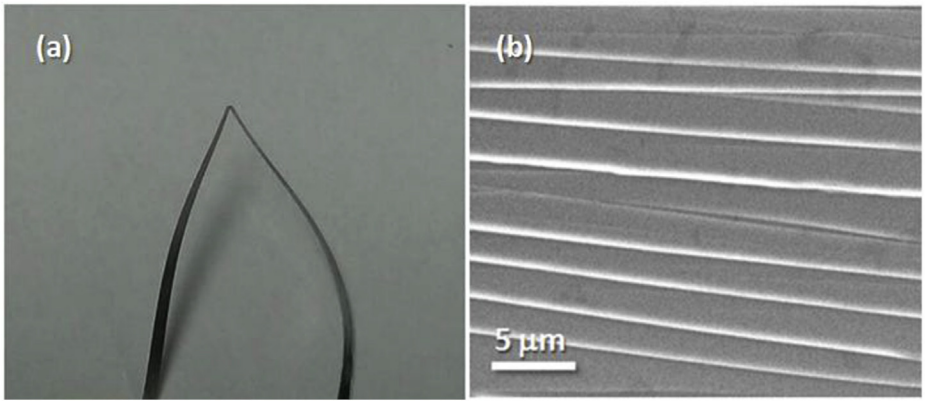

Fig. 4. (a) outer surface and (b) SEM image obtained near the crease mark of the bent alloy ribbon $Fe_{84}Mo_2B_8Si_2P_4$ annealed at 593 K (T_{x1}-100 K) for 600 s.

ductility is maintained even after annealing. As a reference, Fig. 4(a) shows the surface appearance of the $Fe_{84}Mo_2B_8Si_2P_4$ alloy ribbon annealed at 593 K (i. e., T_{x1}-100 K) subjected to the bending deformation through 180°. The ribbon does not crack into two pieces, indicating good bending ductility even after the optimum annealing. In order to examine the deformation behavior in details, the crease marks were observed with a SEM (Fig. 4(b)). The surface shows a number of shear bands, revealing its excellent bending ductility. It is well known that although as-spun Fe-based amorphous alloys are ductile, they become brittle upon annealing at the temperatures well below the onset temperature of crystallization. Nevertheless, it is notable that the present alloy can keep good bending ductility even after annealing.

After annealing at T_{x1}-100 K, Vickers' hardness of the alloys exceeds 900 HV, as listed in Table 1. This value is much higher than the commercialized Fe-Si steel (450 HV), indicating the enhancement in mechanical property. All hysteresis B-H loops exhibit the typical soft magnetic character. Saturation magnetic flux density (B_s) and coercivity (H_c) of these annealed alloy ribbons are summarized in Table 1. Compared with the TM-free alloy compositions, although the addition of the nonmagnetic refractory elements (such as Mo and Cr) could cause the decrease of saturation magnetization in the multicomponent alloys [9], the present alloys still maintain relatively high B_s values, which are much higher than the Cr, Nb-adopted SENNTIX type soft magnetic alloys [5].

Fig. 5(a) shows their polarization curves measured in 3.5 mass% NaCl solution at 298 K. The corresponding electrochemistry parameters such as corrosion potential (E_{corr}) and corrosion current density (I_{corr}) are also listed in Table 2. Their corrosion current density, revealing the corrosion rate during polarization, ranges from 10^{-7} to 10^{-6}A/cm^2, which is recognized to be superior to the common level of Fe-metalloid amorphous alloys (10^{-6}~10^{-5} A/cm^2) [7]. In particular, the Cr-adopted C-free alloy exhibits the lowest I_{corr} value, implying the best corrosion resistance among all alloys in the present study. Previously, it has been intensively investigated that Cr significantly contributes to the formation of passive layer, which protects the Fe-based amorphous alloy from subsequent corrosion [10]. Moreover, the protection effect is dependent on Cr content, i. e., the corrosion rate decreases with increasing Cr content up to 8 at % [11]. Although minor addition of Mo in Fe-Si-B-P alloys results in the improvement of corrosion resistance [12], Mo dissolves even at the lower potential during passivation, and is not able to form the surface passive film [13].

The passivation behavior for the $Fe_{84-x}C_xM_2B_8Si_2P_4$ (M = Cr, Mo; x = 0, 1) alloys was further studied. As is well known, a typical passivation progress consists of (1) the initial active polarization; (2) the formation of passive film; (3) stable passivation state; (4) pitting corrosion, and (5) the damage of passive film [14,15]. Among them, (2) and (4) are the key steps controlling the passivation behavior and have been studied intensively in various kinds of metallic materials [16,17]. In our present study, pitting corrosion behavior has been studied by electrochemistry impedance spectrum (EIS) measurement. Fig. 5(b) shows the Bode plot of the present amorphous alloys. The peak in each curve at low frequency indicates the inoculation of pitting corrosion [6], i. e., distinct peak revealing the serious pitting, while gradual peak suggesting the moderate pitting. It shows clearly that their details of the present alloys in low frequency side are different, indicating their different

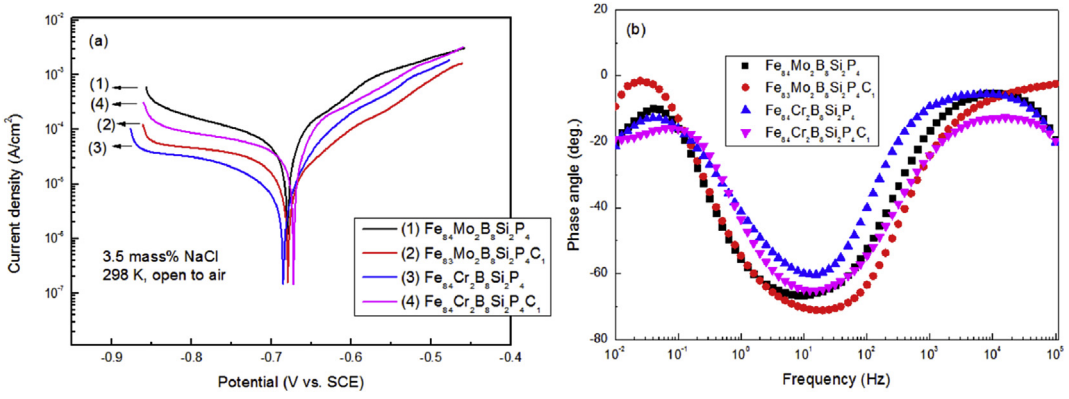

Fig. 5. (a) Polarization curves and (b) Bode plot of impedance spectrum for $Fe_{84-x}C_xM_2B_8Si_2P_4$ (x = 0, 1; M = Mo and Cr) alloy ribbons measured in 3.5 wt% NaCl solution at 298 K.

Table 2
Corrosion potential (E_{corr}) and current density (I_{corr}) of $Fe_{84-x}C_xM_2B_8Si_2P_4$ (x = 0, 1; M = Mo or Cr) alloys in as-spun state and annealed at each T_{x1}-100 K for 600 s.

Composition	E_{corr} (V)	I_{corr} (μA cm^{-2})	E_{corr} (V)	I_{corr} (μA cm^{-2})
	As-spun		Annealed	
$Fe_{84}Mo_2B_8Si_2P_4$	−0.680	6.503	−0.672	0.275
$Fe_{83}Mo_2B_8Si_2P_4C_1$	−0.679	1.536	−0.672	0.344
$Fe_{84}Cr_2B_8Si_2P_4$	−0.685	0.675	−0.676	0.206
$Fe_{83}Cr_2B_8Si_2P_4C_1$	−0.672	2.054	−0.680	0.213

pitting behaviors. Here one can recognize that the Mo-adopted C-containing alloy exhibits the most serious degree of pitting corrosion, while other alloys show the similar extent. The degradation of pitting resistance of the $Fe_{83}Mo_2B_8Si_2P_4C_1$ alloy is presumably due to the dissolution of Mo-containing passive film and the consequent exposure of C atoms in the corrosive environment. It is deduced that these C atoms distributed in the amorphous structure decrease the corrosion resistance though the formation of tiny primary cells, which is similar to the situation in crystalline steel materials.

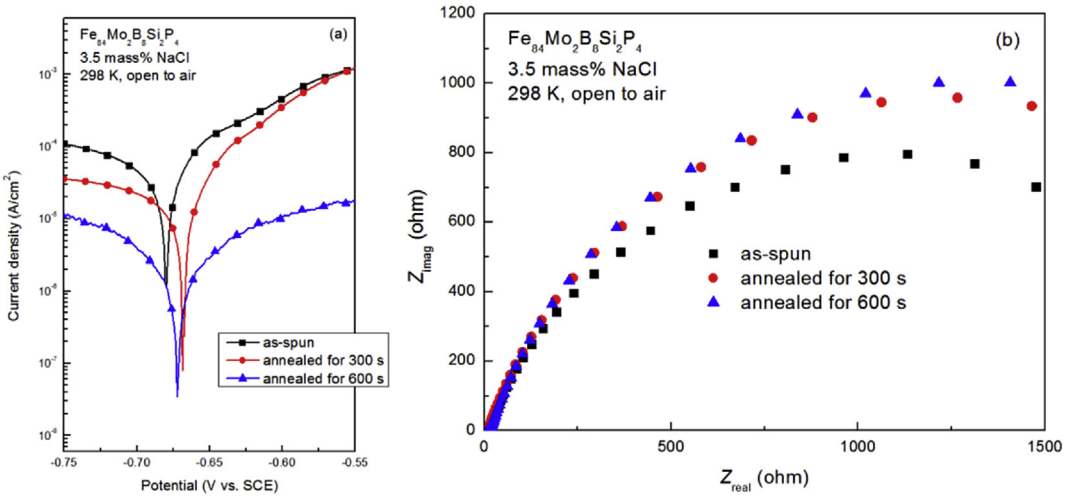

Fig. 6. (a) Polarization curves and (b) Nyquist plots of $Fe_{84}Mo_2B_8Si_2P_4$ alloy in as-spun state as well as annealed at 593 K (T_{x1}-100 K) for 300 s and 600 s.

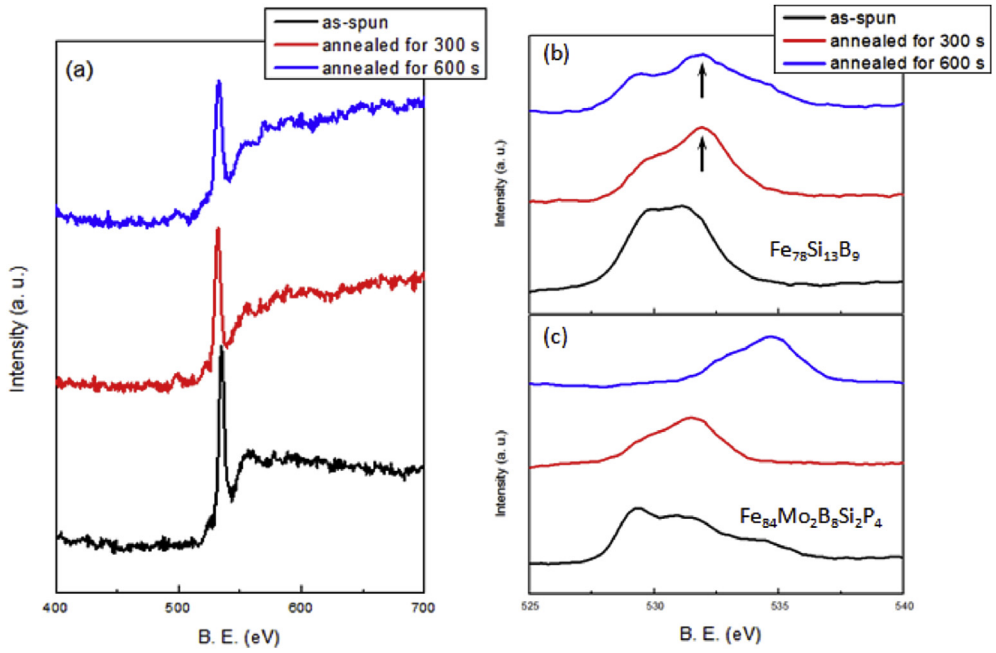

Fig. 7. (a) XPS of $Fe_{84}Mo_2B_8Si_2P_4$ alloy in as-spun state as well as annealed at 593 K (T_{x1}-100 K) for 300 s and 600 s. High resolution XPS spectra of (b) $Fe_{78}Si_{13}B_9$ and (c) $Fe_{84}Mo_2B_8Si_2P_4$ alloy in as-spun state as well as annealed at each (T_{x1}-100 K) for 300 s and 600 s.

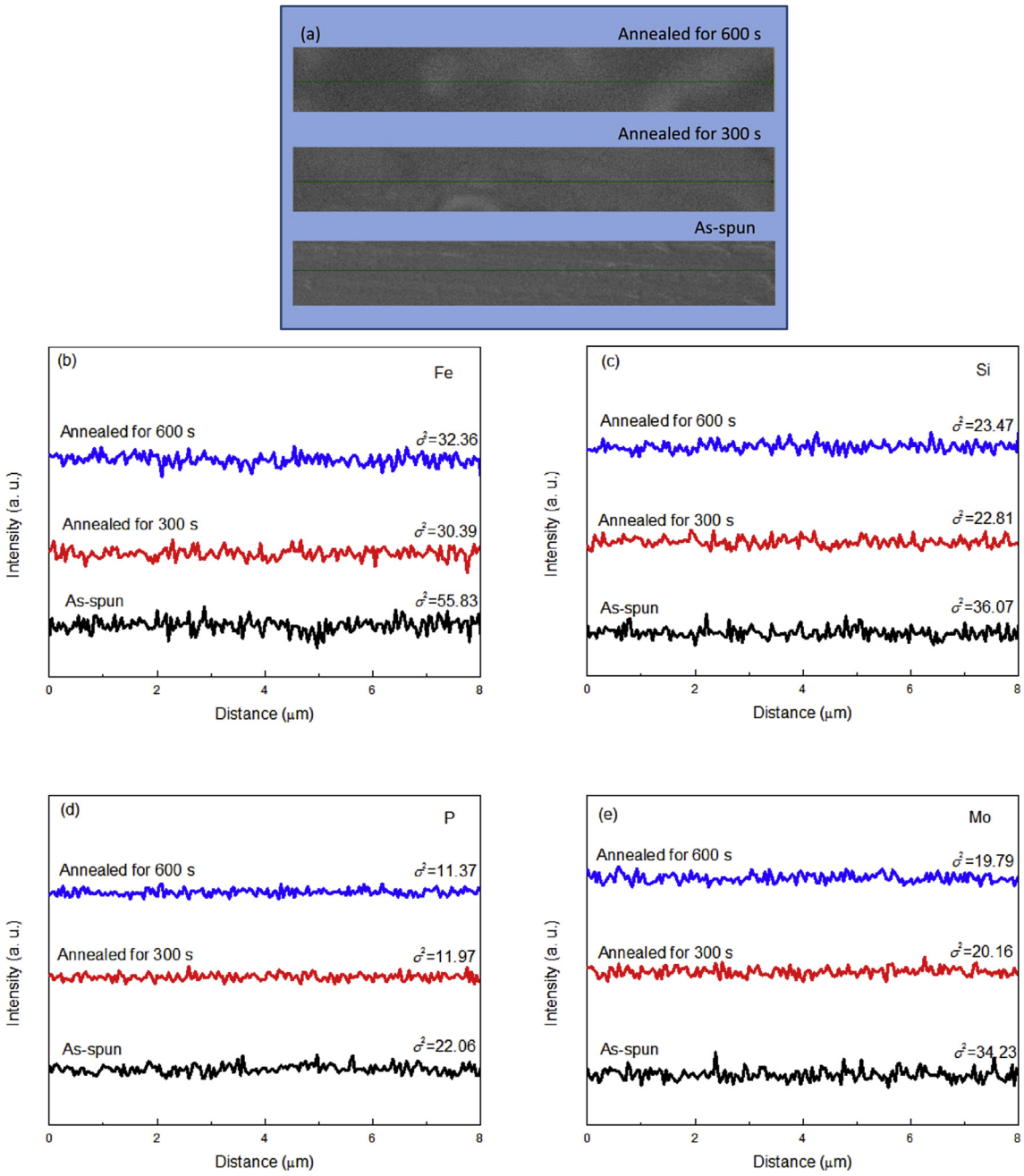

Fig. 8. (a) SEM images and (b)–(e) Fe, Si, P, Mo element EDX spectrum of linear scanning and the corresponding SEM images for $Fe_{84}Mo_2B_8Si_2P_4$ alloy in as-spun state and annealed at 593 K (T_{x1}-100 K) for 300 s and 600 s.

We further investigated the influence of annealing on the corrosion resistance of the present alloys. The current density decreased with increasing annealing time for all the alloys, indicating the decrease of corrosion rate (see Table 2). As exemplified in Fig. 6 for the polarization curves and Nyquist plots of $Fe_{84}Mo_2B_8Si_2P_4$ alloy in different heat treatment state, the corrosion resistance of the alloy is improved upon annealing, as indicated from the decrease in corrosion current density and the increase in charge transfer resistance (the radium).

The annealing-induced improvement of corrosion resistance is attributed to the surface performance. On the contrary, it is known that surface crystallization causes the decrease of corrosion resistance [18–21]. For the present alloys, no crystallization can be recognized after annealing (see Supplementary Fig. 1). This result is due to the increase in thermal stability caused by the addition of Cr or Mo element as well as appropriate choice of annealing condition. Therefore, some factors of surface performance such as surface oxide layer, compositional uniformity and smoothness were investigated to clarify the reason for the improvement of corrosion resistance.

The contribution of surface oxide layer to corrosion resistance was reported by Gravano et al. They studied the influence of heat treatments on the anodic behavior and on the structure of Fe-Ni-based amorphous alloy [22]. A superior performance has been recognized for the specimens annealed for 2 h at 350 °C. The presence of a surface oxide layer has been recognized, which

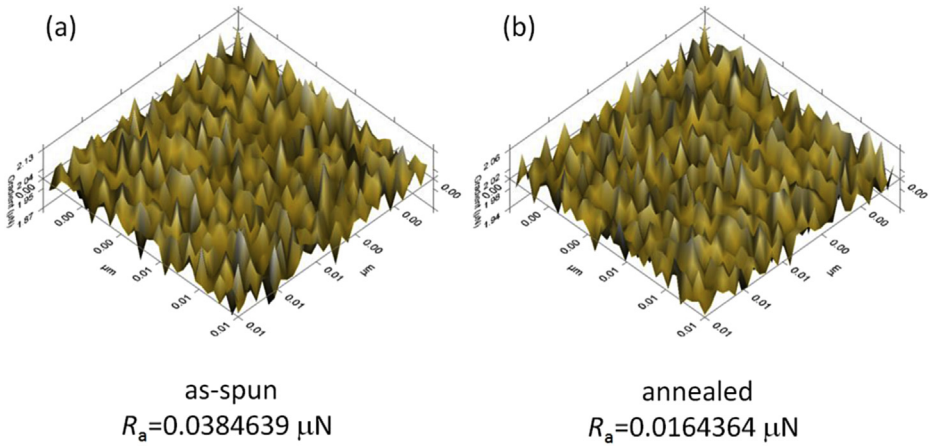

Fig. 9. Simulated AFM images revealing the surface roughness shown in force gradient of $Fe_{84}Mo_2B_8Si_2P_4$ alloy ribbon in (a) as-spun state and (b) annealed at 593 K (T_{x1}-100 K) for 600 s.

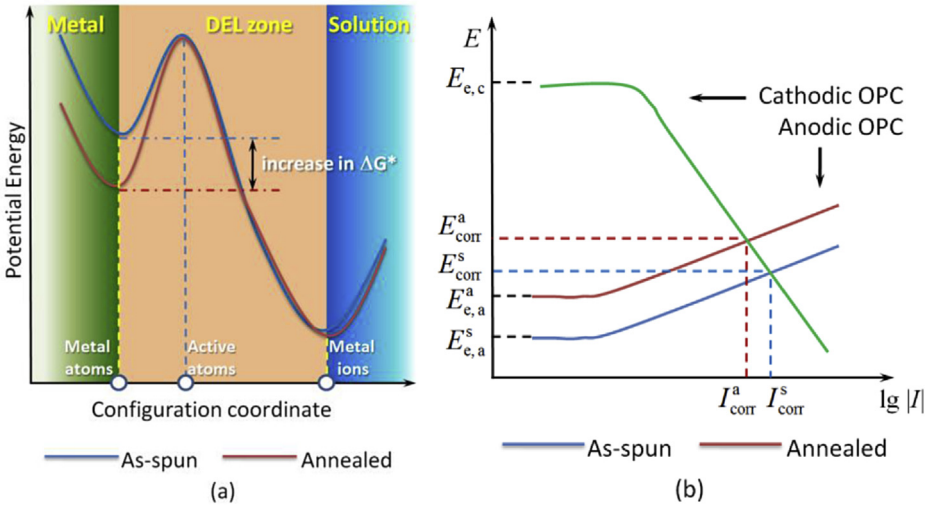

Fig. 10. Schematic diagram of (a) potential energy curves of atoms in different configuration during anodic corrosion. The increase of activation energy (ΔG*) caused by structural relaxation for the process of atom activation in double electric layer (DEL) zone has been revealed. (b) Over potential curves (OPC) of cathodic and anodic electrochemistry reaction implying the improvement of corrosion resistance caused by annealing. Every item marked on the coordinates have the common meaning in electrochemistry. The superscript "s" and "a" stand for "as-spun" and "annealed" states, respectively.

partially affects the corrosion resistance. With the aim of clarifying the influence of oxide layer, the $Fe_{84}Mo_2B_8Si_2P_4$ alloy was studied by XPS. Fig. 7(a) shows the XPS spectra of the $Fe_{84}Mo_2B_8Si_2P_4$ alloy in as-spun and annealed states. The peak of O 1s can be recognized in all spectra, and their estimated contents are in the same magnitude, indicating no obvious change in the surface oxide layer has occurred. Since the similar peaks corresponding to the iron oxide can be recognized in all alloys (not shown here), we obtained the high resolution XPS spectra near O 1s peak of $Fe_{84}Mo_2B_8Si_2P_4$ and $Fe_{78}Si_{13}B_9$ alloys to study the influence of Mo on the formation of oxide layer. As shown in Fig. 7(b), one can recognize the peaks corresponding to SiO_2 and B_2O_3 present in the spectra of annealed $Fe_{78}Si_{13}B_9$ alloys and turn to vanish in that of the $Fe_{84}Mo_2B_8Si_2P_4$ alloys. It is thus concluded that the addition of Mo impedes the formation of silicon- and boron-oxides, implying the improvement of oxidation resistance. This result indicates that the heat treatment does not cause significant change in the level of surface oxide layer before and after annealing. Therefore the annealing-induced improvement of corrosion resistance is not attributed to the changes in surface oxide layer for the present alloys.

In order to clarify the change in surface compositional uniformity, the as-spun and annealed $Fe_{84}Mo_2B_8Si_2P_4$ alloy ribbons were examined by SEM. Fig. 8 shows their SEM images together with the EDX linear scanning spectrum of all the detected elements and their corresponding variance data (σ^2), which reveal the compositional uniformity of the amorphous alloys. No obvious difference in their surface morphology can be recognized between the as-spun and annealed ribbons, indicating that the surface morphology does not change obviously after the present annealing treatment within the sensitivity of SEM. However, the annealed ribbons show lower σ^2 than that of the as-spun ribbon. The above data were obtained from the roll connected surface, and the freely solidified surface also shows the same tendency. The result clearly shows that the composition becomes more homogeneous by means of annealing, in accordance with other researchers' reports [23,24]. The change of compositional uniformity is presumably due to the reduction of internal defects as well as the progress of topological atom rearrangement to form more stable local structures. In addition, no obvious difference in EDX variance can be noticed between the two annealed samples (300 s and 600 s), approaching an

equilibrium state for the atomic configurations after annealing for 300 s.

Fig. 9 shows two simulated images obtained from AFM measurement together with their corresponding average roughness (R_a) calculated from the results. One can easily recognize that the fully annealed alloy exhibits better surface smoothness than that of the as-spun alloy. This result is presumably due to the reduction of the average atom distance in the amorphous structure (see Supplementary Fig. 2). Since the corrosion resistance strongly depends on the surface quality of the material, it is therefore concluded that the improvement of corrosion resistance is due to the improved surface smoothness and the compositional uniformity. This also indicates that the atomic configuration approaches the low-energy equilibrium state by structural relaxation.

From the viewpoint of potential energy, the improvement of corrosion resistance can be explained as follows. The process of corrosion reaction occurs step by step. Considering the general situation, the metal atoms are activated to active atoms in double electric layer (DEL) at the first step. Subsequently, the active atoms transfer to the surface of DEL and then lose their electronics to complete the corrosion reaction. Here the first step (activation of atoms in DEL) is the corrosion rate-determining step, which determines the apparent corrosion resistance of the alloys. Fig. 10(a) shows the potential energy in different atomic coordinations. Since the energy state of active atoms is higher, the atoms in ground state require energy to overcome the energy barrier, which can be regard as the activation energy (ΔG^*) for this process. As discussed above, structural relaxation causes the change in the system energy to a lower state, which leads to the increase of ΔG^*. On the other hand, the equilibrium potential of anode reaction ($E_{e,\ a}$) has a linear relation to ΔG^*: $E_{e,\ a} \propto \Delta G^*/F$. (Here F is the Faraday constant). Thus, as shown in Fig. 10(b), the increase of ΔG^* value causes the increase in $E_{e,\ a}$ of the alloy from as-spun state ($E^s_{e,\ a}$) to annealed state ($E^a_{e,\ a}$), resulting in the upper shift of the anodic over potential curve (OPC). This situation leads to the crossover point of anodic and cathodic OPC (I_{corr}, E_{corr}) shifts to the upper left side, indicating the increase of E_{corr} and decrease of I_{corr}, i. e., the improvement of corrosion resistance caused by structure relaxation.

4. Summary

Fe-Si-B-P-(C) amorphous alloys containing a small amount of Mo or Cr element were synthesized in the present study. These alloys exhibit high saturation magnetic flux density near 1.5 T in conjunction with low coercivity below 10 A/m as well as good bending ductility. By minor-addition of Mo or Cr element, thermal stability, oxidation resistance and corrosion resistance are significantly enhanced in Fe-Si-B-P-(C) alloy system. The combined performance of the present alloys is much superior to those of the commercialized SENNTIX alloys. Moreover, we recognized that the corrosion resistance could be further improved by structural relaxation. The annealing-induced improvement of corrosion resistance is caused by the uniformity of the local composition and the improvement of surface smoothness.

Acknowledgements

The present research is supported by China Postdoctoral Fund (2014M560186), JSPS KAKENHI Grant (26630299) in Japan, Recruitment Program of Global Experts “1000 Talents Plan” of China (WQ20121200052) and Deanship of Scientific Research (DSR), King Abdulaziz University, Jeddah, Saudi Arabia (1-1-1435/HiCi).

Appendix A. Supplementary data

Supplementary data related to this article can be found at http://dx.doi.org/10.1016/j.intermet.2016.05.011.

References

[1] D.C. Jiles, Acta Mater 51 (2003) 5907–5939.
[2] A. Inoue, F.L. Kong, Q.K. Man, B.L. Shen, R.W. Li, F. Al-Marzouki, J. Alloys Compd 615 (2014) S2–S8.
[3] H. Matsumoto, A. Urata, Y. Yamada, A. Inoue, IEEE Trans. Magn 46 (2010) 373–376.
[4] H. Koshiba, Y. Naito, T. Mizushima, A. Inoue, Mater. Jpn. 47 (2008) 39–41.
[5] H. Matsumoto, A. Urata, Y. Yamada, A. Inoue, J. Alloys Compd. 509 (S1) (2011) S193–S196.
[6] Y. Han, C.T. Chang, S.L. Zhu, A. Inoue, D.V. Louzguine-Luzgin, E. Shalaan, F. Al-Marzouki, Intermetallics 54 (2014) 169–175.
[7] Y. Han, F.L. Kong, C.T. Chang, S.L. Zhu, A. Inoue, E. Shalaan, F. Al-Marzoki, J. Mater. Res. 30 (2015) 547–555.
[8] F.L. Kong, C.T. Chang, A. Inoue, E. Shalaan, F. Al-Marzouki, J. Alloys Compd. 615 (2014) 163–166.
[9] P. Pawlik, H.A. Davies, J. Non Cryst. Solids 329 (2003) 17–21.
[10] S.J. Pang, T. Zhang, K. Asami, A. Inoue, Mater Trans. 43 (2002) 2137–2142.
[11] Z.L. Long, Y. Shao, X.H. Deng, Z.C. Zhang, Y. Jiang, P. Zhang, B.L. Shen, A. Inoue, Intermetallics 15 (2007) 1453–1548.
[12] X. Li, C.L. Qin, H. Kato, A. Makino, A. Inoue, J. Alloys Compd. 509 (2011) 7688–7691.
[13] M.W. Tan, E. Akiyama, H. Habazaki, A. Kawashima, K. Asami, K. Hashimoto, Corr. Sci. 38 (1996) 2137–2154.
[14] C.N. Cao, Principles of Electrochemistry of Corrosion, Chemical Industry Press, 2008, pp. 216–219.
[15] C. Suryanarayana, A. Inoue, Bulk Metallic Glasses, CRC Press, 2011, pp. 309–312.
[16] A. Baron, D. Szewieczek, G. Nawrat, Electrochem. Acta 52 (2007) 5690–5695.
[17] Y. Han, Z.D. Cui, Q. Wei, S.L. Zhu, X.J. Yang, Adv. Mater. Res. 457–458 (2012) 358–364.
[18] H.M.M.N. Hennayaka, H.S. Lee, S.H. Yi, J. Alloys Compd. 618 (2015) 269–279.
[19] G.Y. Koga, R.P. Nogueira, V. Roche, A.R. Yavari, A.K. Melle, J. Gallego, C. Bolfarini, C.S. Kiminami, W.J. Botta, Surf. Coat. Tech. 254 (2014) 238–243.
[20] H. Zohdi, M. Bozorg, R. Arabi Jeshvaghani, H.R. Shahverdi, S.M.M. Hadavi, Mater. Lett. 94 (2013) 193–196.
[21] Y. Yang, C. Zhang, Y. Peng, Y. Yu, L. Liu, Corr. Sci. 59 (2012) 10–19.
[22] S.M. Gravano, S. Torchio, E. Angelini, C. Antonione, M. Baricco, Corr. Sci. 32 (1991) 509–519.
[23] Y.Y. Zhao, A. Inoue, C.T. Chang, J. Liu, B.L. Shen, X.M. Wang, R.W. Li, Sci. Rep UK 4 (2014) 5733.
[24] W.M. Yang, J.W. Li, H.S. Liu, C.C. Dun, H.L. Zhang, J.T. Huo, L. Xue, Y.C. Zhao, B.L. Shen, L.M. Dou, A. Inoue, Intermetallics 49 (2014) 52–56.